Catalysis Today 178 (2011) 85–97

Contents lists available at ScienceDirect

Catalysis Today

journal homepage: www.elsevier.com/locate/cattod

Microstructure formation on exposure of silicon carbide surfaces to the partial oxidation of methane

Woo Jin Lee[a], Chao'en Li[a], Benny Kuan[b], Nick Burke[a], Karl Gerdes[c], Jim Patel[a,*]

[a] CSIRO Earth Science and Resource Engineering, Ian Wark Laboratory, Bayview Avenue, Clayton, Victoria 3168, Australia
[b] CSIRO Mathematics, Informatics and Statistics, Clayton South, Bayview Avenue, Clayton, Victoria 3168, Australia
[c] Process Engineering Division, Chevron Energy Technology Company, 100 Chevron Way, Richmond, CA 94802, USA

ARTICLE INFO

Article history:
Received 23 May 2011
Received in revised form 14 July 2011
Accepted 14 July 2011
Available online 12 August 2011

Keywords:
Silicon carbide
Corrosion
Microstructures
Core–shell fibres
Silicon oxide
Graphite

ABSTRACT

Gas-phase silicon-based species, produced on exposure of silicon carbide (SiC) surfaces to the partial oxidation of methane, can be transported away from the site of corrosion to form surface nano- and microstructures. These structures can be divided into two groups, silicon-based structures and silicon/carbon-based structures. Silicon oxide nanowires are the most prevalent of the silicon-based structures, and form on SiC surfaces downstream of the combustion zone. The silicon/carbon-based structures, formed towards the end of the combustion zone, are core–shell heterostructured fibres and take the form of either conical fibres or cross-linked fibre lattices. Low reactive gas concentrations, high temperatures and low methane/oxygen ratios enhance microstructure formation. The effect of gas-phase chemistry and fluid flow on surface behavior is discussed.

1. Introduction

Silicon carbide (SiC) is a high performance ceramic that shows excellent durability in a range of severe operating conditions. SiC also possesses a number of highly desirable properties including high thermal conductivity, excellent thermal shock resistance, low chemical reactivity and high mechanical strength. These characteristics have led to SiC being used in a range of applications. Previous studies have proposed various types of reactors based on SiC for high temperature processes involving hydrocarbons, including conventional fixed bed reactors [1], honeycomb reactors [2], solar driven reactors [3], membrane reactors [4] and micro-structured reactors [5,6]. One application for which SiC holds promise is as a support material for heterogeneous catalysts [7], in particular for oxidation and partial oxidation applications [5,8–10]. For these processes carbon formation inside the reactor can be problematic, and has the potential to interrupt long-term operation. For example, even minor changes on the surface of an inner wall in a microreactor have the potential to compromise the performance of the reactor. To maximize the performance of reactors, the behavior of the SiC surface under such harsh environments should be clearly understood. In this report we describe an investigation into the use of SiC as a reactor material for the partial oxidation of methane (POM). At the commencement of this study it appeared likely that the presence of catalytically active metal species would significantly complicate the behavior of the surface on exposure to the POM. We therefore set out to gain an understanding of the behavior in the absence of catalytic materials. During this study we found that in some circumstances silicon and carbon based microstructures can form on SiC surfaces exposed to the POM. The growth and morphology of these unusual core–shell fibre structures have been described in two preliminary communications [11,12]. In this paper we describe an extension of these studies in which we have conducted a systematic investigation into the effect of process variables on the behavior of SiC surfaces exposed to the POM and the formation of silicon and carbon based microstructures. Focused on the fuel rich conditions under which the microstructures form, we have investigated the effect of the methane to oxygen ratio, process temperature, water and hydrogen addition to the feed and the residence time. In addition to our experimental investigation we have conducted a combination of computational fluid dynamics and kinetic simulations to probe the relationships between gas-phase processes and surface effects.

---

* Corresponding author. Tel.: +61 3 9545 8356; fax: +61 3 9545 8380.
E-mail addresses: WooJin.Lee@csiro.au (W.J. Lee), Chaoen.Li@csiro.au (C. Li), Benny.Kuan@csiro.au (B. Kuan), Nick.Burke@csiro.au (N. Burke), Karl.Gerdes@chevron.com (K. Gerdes), Jim.Patel@csiro.au (J. Patel).

0920-5861/$ – see front matter. Crown Copyright © 2011 Published by Elsevier B.V. All rights reserved.
doi:10.1016/j.cattod.2011.07.012

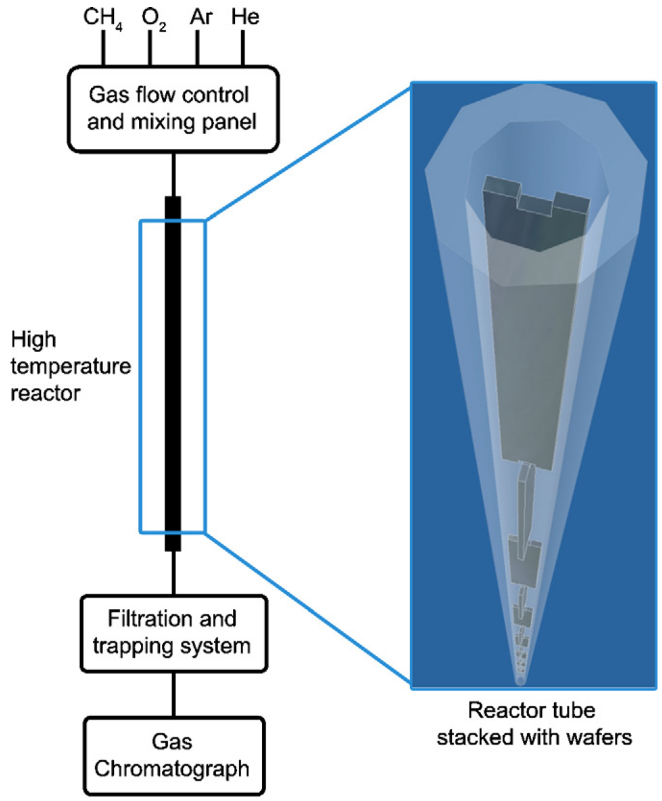

Fig. 1. A schematic diagram of the reactor setup.

2. Materials and methods

2.1. Exposure of SiC surfaces to the partial oxidation of methane (POM)

A gas flow control and mixing panel was supplied with methane (Linde, 99.95%), oxygen (Linde, 99.9%), hydrogen (BOC, 99.99%), helium (BOC, 99.99%) and argon (BOC, 99.99%). The gas flow rates were controlled by mass flow controllers (Brooks 5850E) operating within the range of 10–90% of their total flow (Fig. 1). Each of the mass flow controllers was calibrated with a Bios Definer 220 flow meter and calibration curves were checked for linearity. Water was injected into the reactor tube at a point where the temperature exceeded 200 °C through a 1/16″ i.d. stainless steel tube using an ISCO syringe pump (500D). The feed and exit gas pressures were monitored by pressure transducers. The gases were mixed prior to being fed into the high temperature reactor.

Gas chromatography was used for quantitative analysis of the feed and product streams with an on-line Shimadzu GC17A chromatograph set up with two flow lines. A sample of the product stream was simultaneously injected into each flow line and two analyses were conducted concurrently. One flow line, equipped with a Varian CP-Molsieve 5A column (25 m, 0.53 mm, 50 μm) and a thermal conductivity detector, was used for the analysis of helium, hydrogen and oxygen, with argon as the carrier gas. The second flow line, equipped with a Varian CP-PoraPLOT Q column (27.5 m, 0.53 mm, 20 μm), methaniser and flame ionisation detector, was used for the analysis of carbon dioxide, carbon monoxide and C_1–C_3 hydrocarbons, with helium as the carrier gas. Analyses were conducted under isothermal conditions at 30 °C. Product gas compositions were determined with reference to a series of calibration curves, which were constructed from the analysis of five standard gas mixtures. Based on an error analysis of the experimental system (gas flow control and analysis of products), the relative experimental error for each of the gaseous products was calculated to be: CH_4, 6%; O_2, 8%; He, 7%; H_2, 8%; CO, 7%; CO_2, 7%; C_2H_2, 6%; C_2H_4, 6%; C_2H_6, 6%; Ar, 6%. Analyses of the product gas were performed every 10 min for each of the experiments conducted. In all cases the product gas compositions did not change, outside of experimental error, throughout the exposure period. The results reported are an average of three separate analyses.

The reactor consisted of a sintered α-SiC tube (Length 900 mm, i.d. 6 mm, Hexloloy-SA, Saint Gobain). The tube was heated in an electrical furnace. The reactor was designed as a down-flow reactor with a filtration and trapping assembly located on the reactor outlet. The stainless steel fittings and sections of the reactor tube housed outside the furnace were fan-cooled.

Longitudinal temperature profiles within the reactor were measured using an S-type sliding thermocouple, without SiC wafers inside the reactor, under both non-reactive conditions and conditions identical to those used in the actual reactions.

Typically, experiments were conducted as follows. A set of 16 ceramic wafers (pressureless sintered α-SiC) of 50 mm $(L) \times 4.75$ mm $(W) \times 0.72$ mm (D) (Cerametec Co., USA) were cleaned using iso-propanol, oven dried at 328 K, allowed to cool to ambient temperature and then weighed. The wafers were stacked in the reactor tube as shown in Fig. 1. All axial positions within the reactor are quoted relative to the inlet of the reactor tube (0 mm). Wafers were stacked from 261 mm to the outlet of the reactor tube.

The notches in the upper and lower edges of the wafers (Fig. 1) were used to connect the wafers and ensure that adjoining wafers were perpendicular to one another. The reactor was heated at 100 °C h^{-1} from room temperature to the furnace set temperature under a flow of argon (150 sccm). Once the furnace reached the desired temperature, the reactive gas stream was fed into the reactor. The product gas was analyzed by gas chromatography at 10-min intervals. The reactant gas flow was maintained for a period of 4 h. After this time the reactant gases were removed from the feed and the argon flow rate was reduced to 150 sccm. The reactor was cooled to room temperature at a rate of 100 °C h^{-1}. Once cooled, the reactor was disassembled and the wafers weighed. A summary of the experiments conducted is presented in Table 1.

2.2. Analysis of wafer surfaces

The surfaces of the SiC wafers were analyzed by scanning electron microscopy (SEM; FE-SEM Philips XL30 and JEOL JSM 7001F FEG-SEM) combined with energy disperse X-ray spectroscopy (EDXS), micro-Raman spectroscopy (Reinshaw Invia, $\lambda_0 = 514.5$ nm) and 3D Surface Area Structure Analysis (Altimet 500).

2.3. Modeling

2.3.1. Computational fluid dynamics (CFD) simulations

Two CFD models of the laboratory-scale tubular reactors: one with and the other without wafers were developed. Single-phase, steady state flow simulations were performed using a commercial CFD code ANSYS CFX-11. The simulation involved numerically solving the following set of Reynolds-Averaged Navier–Stokes (RANS) and transport equations:

Continuity

$$\nabla \cdot (\rho \mathbf{U}) = 0 \tag{1}$$

RANS

$$\nabla \cdot (\rho \mathbf{U}\mathbf{U}) - \nabla \cdot (\mu \nabla \mathbf{U}) = -\nabla P + \nabla \cdot \sigma^T \tag{2}$$

where **U** is mean velocity vectors, ρ density, P pressure, μ molecular viscosity, and σ^T Reynolds stresses.

Table 1
The experimentally determined and simulated gas phase compositions for the conditions tested.

Experiment # Expt./simulation	A Expt. (sim)	B Expt. (sim)	C Expt. (sim)	D Expt. (sim)	E Expt. (sim)	F Expt. (sim)	G Expt. (sim)	H Expt. (sim)	I Expt. (sim)
Time (min)	240	240	240	240	240	240	240	240	48
Furnace temp. (°C)	1400	1400	1400	1350	1450	1400	1400	1400	1400
Feed (%)									
CH_4	1.00	1.00	1.00	1.00	1.00	1.00	1.00	1.00	10.0
O_2	0.90	0.63	0.48	0.63	0.63	0.63	0.63	0.90	9.00
He	1.00	1.00	1.00	1.00	1.00	1.00	1.00	1.00	5.00
H_2	0.00	0.00	0.00	0.00	0.00	1.00	0.00	0.00	0.00
H_2O	0.00	0.00	0.00	0.00	0.00	0.00	10.00	0.00	0.00
Ar	97.1	97.4	97.5	97.4	97.4	96.4	87.4	97.1	76.0
Flow rate (sccm)[a]	5000	5000	5000	5000	5000	5000	5000	2000	5000
Feed CH_4/O_2	1.11	1.60	2.10	1.60	1.60	1.60	1.60	1.11	1.11
Gas product (%)									
CH_4	0.04 (*0.01*)	0.08 (*0.08*)	0.13 (*0.19*)	0.17 (*0.21*)	0.05 (*0.05*)	0.15 (*0.12*)	0.13 (*0.03*)	0.06 (*0.01*)	1.79 (*1.93*)
O_2	0.00 (*0.00*)	0.00 (*0.00*)	0.00 (*0.06*)	0.00 (*0.15*)	0.00 (*0.01*)	0.00 (*0.01*)	0.00 (*0.00*)	0.00 (*0.00*)	0.00 (*1.60*)
He	1.02 (*1.00*)	1.09 (*1.00*)	1.05 (*1.00*)	0.96 (*1.00*)	0.96 (*1.00*)	1.01 (*1.00*)	1.04 (*1.10*)	2.03 (2.00)	3.44 (*5.39*)
H_2	1.00 (*1.03*)	1.11 (*1.07*)	1.11 (*1.01*)	0.95 (*0.88*)	0.95 (*1.11*)	1.73 (*1.80*)	1.11 (*1.75*)	0.98 (1.04)	12.2 (*15.6*)
CO	0.67 (*0.77*)	0.47 (*0.54*)	0.34 (*0.39*)	0.53 (*0.42*)	0.47 (*0.57*)	0.35 (*0.44*)	0.33 (*0.10*)	0.73 (*0.75*)	6.30 (*15.9*)
CO_2	0.09 (*0.08*)	0.04 (*0.03*)	0.02 (*0.02*)	0.05 (*0.03*)	0.05 (*0.03*)	0.03 (*0.02*)	0.11 (*0.22*)	0.28 (*0.10*)	1.51 (*0.52*)
C_2H_2	0.09 (*0.06*)	0.17 (*0.15*)	0.20 (*0.17*)	0.18 (*0.13*)	0.18 (*0.16*)	0.18 (*0.20*)	0.12 (*0.10*)	0.04 (*0.07*)	1.64 (*0.39*)
C_2H_4	0.00 (*0.00*)	0.00 (*0.01*)	0.00 (*0.02*)	0.00 (*0.02*)	0.00 (*0.00*)	0.00 (*0.00*)	0.00 (*0.00*)	0.00 (*0.00*)	0.07 (*0.26*)
C_2H_6	0.00 (*0.00*)	0.00 (*0.00*)	0.00 (*0.01*)	0.00 (*0.01*)	0.00 (*0.00*)	0.00 (*0.00*)	0.00 (*0.00*)	0.00 (*0.00*)	0.00 (*0.04*)
Ar	97.1 (*97.05*)	97.0 (*97.09*)	97.1 (*97.15*)	97.2 (*97.16*)	97.1 (*97.07*)	96.6 (*96.41*)	97.2 (*97.16*)	95.9 (*96.03*)	73.0 (*78.31*)
Conv. (%)									
CH_4	99 (*100*)	92 (*92*)	88 (*81*)	86 (*79*)	95 (*95*)	86 (*88*)	83 (*97*)	94 (*99*)	71 (*80*)
O_2	100 (*100*)	96 (*96*)	100 (*87*)	100 (*76*)	100 (*99*)	100 (*99*)	100 (*99*)	99 (*100*)	100 (*83*)

Text in italics represents simulated results.

[a] Pressure of 70 kPa.

Static enthalpy transport

$$\nabla\cdot(\rho\mathbf{U}h)=\nabla\cdot(\lambda\nabla T)+\mathbf{U}\cdot\nabla P+\tau:\nabla P \tag{3}$$

where h denotes static enthalpy and λ thermal conductivity.

The application of Reynolds-averaging on the Navier–Stokes equations produces a set of nine unknown correlations, which are known as the Reynolds stress tensors σ^T. The present simulation utilised eddy-viscosity hypothesis to relate the Reynolds stresses to mean velocity gradients and eddy viscosity μ_t.

A k–ω based turbulence model: Shear Stress Transport (SST) model of Menter and Esch [13] has been selected and applied to provide a solution for turbulence quantities k and ω. The SST model is known for its capability to predict flows with adverse pressure gradient or separation more accurately than other two-equation turbulence models [14], and has been successfully applied to narrow channel flows [15].

In addition to the transport of static enthalpy, which is directly related to convective transfer of heat within the fluid domain, this study included the effect of thermal radiation. This was accomplished through the use of a 'Discrete Transfer' model, which traced the paths of multiple rays leaving the surfaces bounding the fluid domain. Upon reaching another boundary surface, the ray was assumed to be reflected uniformly in all directions from its point of contact on the surface. Conduction heat transfer through the reactor tube as well as the wafer stacking was also considered in the model.

The simulations considered either nitrogen or argon as a working medium, and a number of operating conditions as tested in the laboratory experiments. The cases without wafers correspond to experiments in which temperatures inside a wafer-free reactor were measured with a thermocouple. The simulation results suggested a dominant influence of radiant heat transfer on the thermocouple readings. At low flow rate (i.e. 1000 sccm), the thermocouple in essence measured temperature that would have been reached on surfaces of the wafers had they been inside the tubular reactor. At high flow rates (i.e. 5000 sccm) the thermocouple readings reflected the gas temperature near the wafers within a ±100 °C band. The simulation also indicated that there was little difference between wafer temperatures at different gas flow rates. The wall temperature profile, as predicted by the CFD simulation was then used subsequently in kinetic modeling.

2.3.2. Kinetic simulations

Kinetic simulations were carried out using the commercial kinetic modeling software package, CHEMIKIN-Pro. Simulations were conducted using a plug flow reactor model with fixed temperature profiles and a combustion mechanism reported by Skjøth-Rasmussen et al. [16]. This mechanism, which consists of 159 species and 773 fundamental chemical reactions, was developed for the fuel rich combustion of methane and incorporates detailed pathways for the production and consumption of polycyclic aromatic hydrocarbons (PAHs). Preliminary simulations demonstrated that this mechanism better simulated the production of C_2 hydrocarbons than GRI-Mech 3.0 [17]. In all simulations a constant pressure was applied. Temperature profiles were generated with reference to temperature profiles measured in the reactor, without wafers, and the temperature profiles produced by CFD modeling. Experimental tests and simulations demonstrated that for the experiments conducted with 1% methane, there was very little difference between the reactor temperatures for each of the conditions tested.

3. Results and discussion

3.1. The effect of selected process variables on gas-phase chemistry

In order to systematically investigate the effect of individual process variables, experiments were conducted with low reactive gas concentrations diluted in argon. The extent of dilution and the gas flow rate were chosen to ensure that significant conversion of methane was achieved and that the heat of the reaction did not contribute significantly to the temperature within the reactor. On the basis of temperature profiles recorded with and without reactive gases it was found that these criteria were met with a total feed gas flow rate of 5000 sccm and methane feed concentration of 1%. Details of the conditions tested and the experimentally determined, and simulated, product gas compositions are presented in Table 1.

3.1.1. *CFD simulations of the fluid flow*

In order to understand the nature of the fluid flow within the reactor, and to determine whether it had any effect on the microstructure formation on the reactor surfaces, a series of CFD simulations was conducted. The vertical SiC wafer stack occupied a substantial space along the reactor tube's centre axis. Due to this obstruction, and the heating of the gas flow as it passed over the wafer surfaces, this stack induced a non-uniform flow pattern. This aided the mixing of the hot and cold gases, but at the same time unevenly distributed gas to the wafer surfaces, potentially affecting the surface structures.

A CFD model of the reactor was developed to provide some insights on the prevailing gas dynamics. The CFD simulation indicated a complex secondary flow structure arising from the SiC wafers that were cross-stacked in the direction of the primary flow. Fig. 2a plots gas velocity vectors on one of the reactor centre-planes near a joint. Directly downstream of a previous wafer, the plot reveals weak flow regions on both faces of the following wafer regions enclosed by dashed lines. The gas streams leaving the edges of the previous wafer then rapidly re-attach to the faces of the following wafer. This is followed by development of a boundary layer on the wafer surfaces as characterized by parabolic velocity profiles further below the joint.

It is worth noting that, existence of these boundary layers leads to a slower gas flow near the centre axis and along the tube wall. The same trend also exists on the surface of the wafers where the surface flow is slower near the centre and faster along the sides.

In the process of the flow-surface re-attachment, gas flow on either side of the centre-plane is entrained by the re-attaching gas stream forming a pair of stream wise vortices along each wafer face. This secondary flow pattern is illustrated in Fig. 2b. In addition to the gas streamlines, the cross-sections are coloured by gas velocities. It is interesting to note that the combination of wafer cross-stacking and flow-surface re-attachment produces a series of vortex systems, which reverse directions from one wafer to the next. These vortex systems are found to enhance mixing between the hot/cold and fast/slow gas streams.

3.1.2. *Kinetic simulations of the gas-phase chemistry*

The CFD modeling indicated a low turbulence level inside the reactor. The predicted gas flow structure was self-similar along a large portion of each wafer, except near the joints. It was thus reasonable to utilise a plug-flow assumption in kinetic modeling (*vide supra*).

On inspection of the experimental and simulated gas phase product compositions in Table 1, it is clear that both hydrogen and carbon monoxide were reasonably well predicted, in essence within experimental error. Both acetylene and carbon dioxide were found to be slightly under predicted, for the latter this was the opposite to what was found by Skjøth-Rasmussen et al. [16]. The oxygen concentration was over predicted at higher temperatures, but the oxygen analysis was not very sensitive and hence there is some uncertainty in the experimental results at low concentrations. Overall the simulations provided a reasonable indication of the gas-phase chemistry within the reactor. Fig. 3 shows simulated mole fractions of selected species in the gas-phase along the reactor for Expts. A–I.

For all experiments, combustion began beyond ca. 420 mm along the reactor, where the temperature reached was ca. 1150 °C. As would be expected, the methane and oxygen were more rapidly consumed in Expts. A and E, which represented the lowest CH_4/O_2 ratio (1:1) and the highest temperature (1450 °C), respectively. With an understanding of the gas composition along the reactor, it was possible to relate surface behavior and gas-phase chemistry. This will be described in detail in Section 3.2.

3.2. *The effect of process variables on SiC surface structures*

The experiments A–I were designed such that comparison of different experiments within the set would allow the effect of different process variables on the SiC surface behavior to be determined.

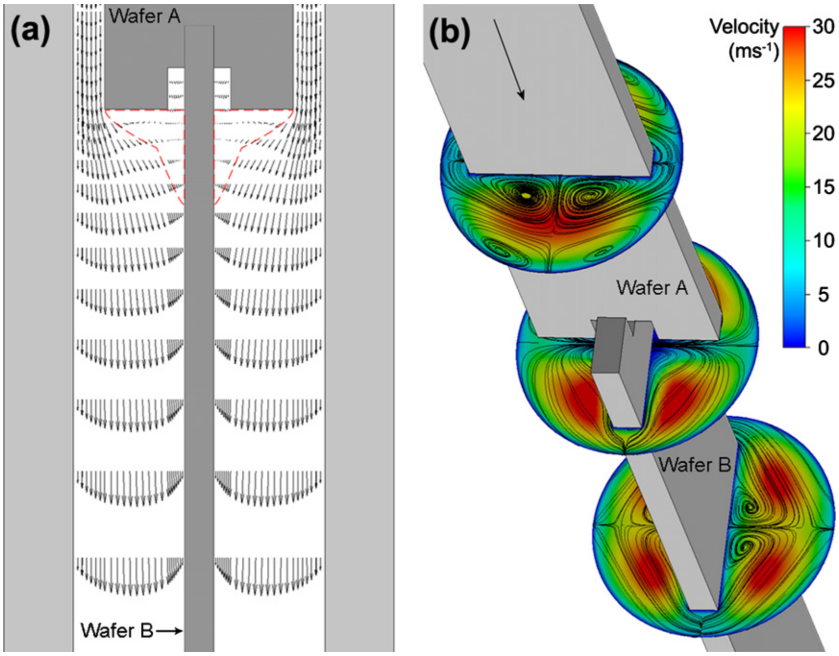

Fig. 2. The predicted gas flow patterns near a joint inside the hot zone. (a) The primary flow represented by velocity vectors on reactor centre-plane; (b) the secondary flow as represented by gas streamlines at selected cross-sections along a wafer.

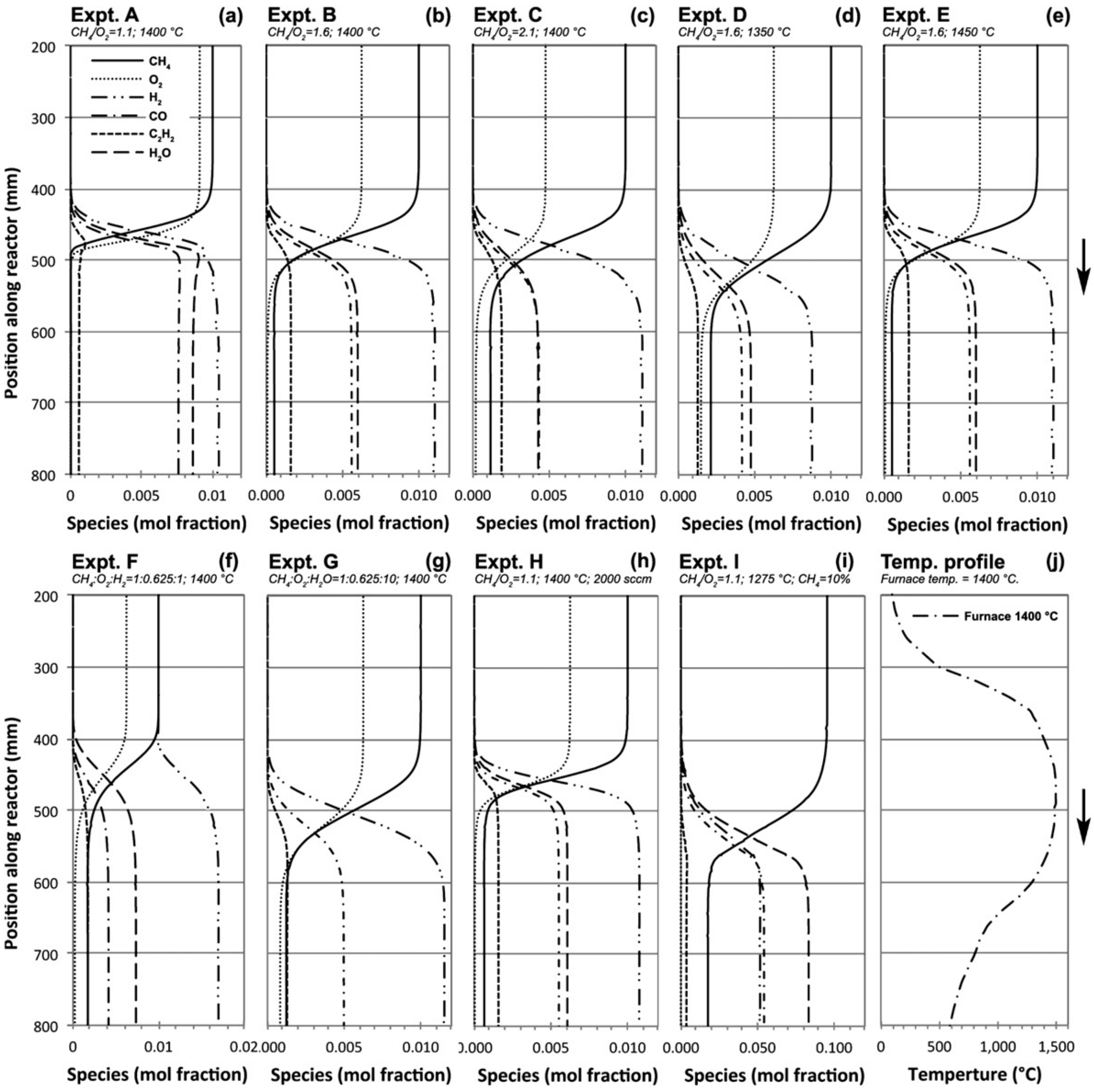

Fig. 3. (a)–(i) The simulated mole fraction of selected species in the gas-phase between 200 and 800 mm along the reactor for Expts. A–I. (j) The temperature profile within the reactor with the furnace temperature set at 1400 °C.

Below each of the following process variables were considered separately: CH_4/O_2 feed ratio; temperature; additives (water and hydrogen); residence time; concentration and fluid flow. However, in Section 3.2.1 we will first describe in general terms the nature of the surfaces observed along the reactor, and suggest possible mechanisms by which these surfaces may have evolved.

3.2.1. *Microstructures formed on SiC surfaces*

SEM analysis of the wafer surfaces from Expts. A–C revealed that as a consequence of exposure to the combustion process, and the associated temperatures, a variety of structures formed depending upon the position along the reactor (Fig. 4).

The first feature of note on the wafer surfaces upstream of the reaction zone was corrosion of the SiC surfaces (Fig. 4a). Areas of pitting, often circular in shape, were found on wafer surfaces which had been heated to above ca. 1150 °C. As can be seen in Fig. 3, in the region where corrosion was observed, between ca. 400 and 450 mm, both the reactor temperature (Fig. 3j) and the oxygen partial pressure (Fig. 3a) were relatively high. Beyond ca. 450 mm the oxygen partial pressure dropped as a result of reaction with methane. Silica, the native oxide of SiC, is well known to form a protective layer over SiC surfaces, and under the conditions examined in this study would have formed by passive oxidation of the SiC surface according to Eq. (4) [18].

$$2SiC_{(s)} + 3O_{2(g)} \rightarrow 2SiO_{2(s)} + 2CO_{(g)} \quad (4)$$

Loss of material from the wafer surface presumably occurred by reaction of the silica layer with gas-phase reductants, such as hydrogen and methane, or by reaction at the SiO_x/SiC interface, as shown for silica in Eq. (5).

$$2SiO_{2(s)} + SiC_{(s)} \rightarrow 3SiO_{(g)} + CO_{(g)} \quad (5)$$

Surface area analysis of the circular holes showed that they had an approximately flat base with a diameter-to-depth ratio of ca. 400, and a deeper pit at the centre (Fig. 5). To account for the holes in this region, we propose that they formed as a result of the crystallization of a surface silica layer. The size and shape of the holes was consistent with β-cristobalite radialites, a crystalline form of silica known to form on SiO_2/SiC surfaces exposed to high temperatures [19]. The loss of SiO_x, which led to the formation of the holes, may have occurred by either reaction at the SiO_2/SiC interface, or on reaction with gas-phase reductants (*vide supra*). The latter could

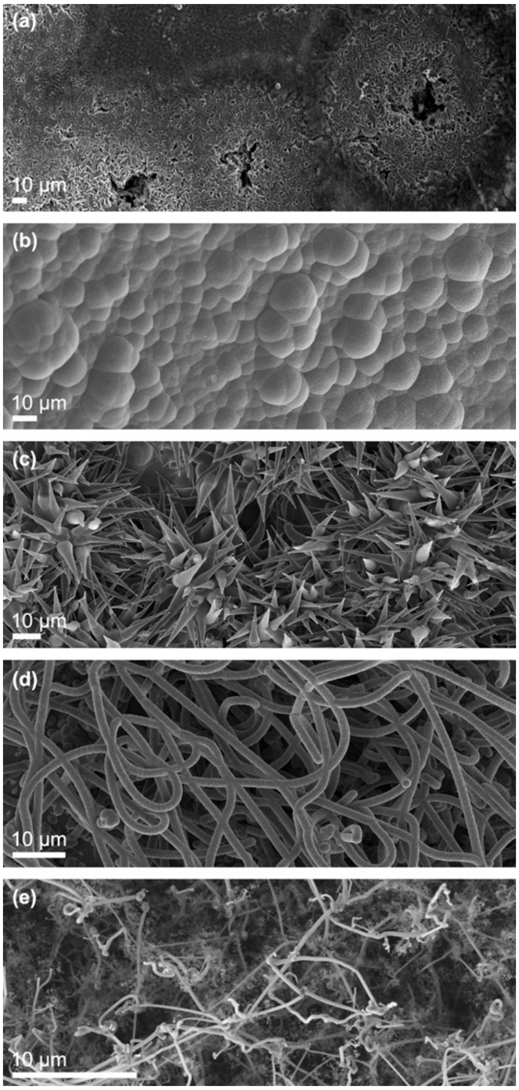

Fig. 4. Features observed on the SiC wafer surfaces along the reactor. (a) SiC corrosion at ca. 420 mm, Expt. A. (b) “Cobbled” carbon at ca. 570 mm, Expt. B. (c) Conical carbon fibres (CCFs) at ca. 600 mm, Expt. C. (d) Carbon fibre lattices at ca. 610 mm, Expt. A. (e) Silicon oxide nanowires at ca. 630 mm, Expt. A.

only have occurred during the combustion period, whereas the former may have occurred during the cooling period when no reactive gas-phase species were present.

Downstream of the corrosion region the wafers were covered by “cobble” like surfaces (Fig. 4b), which EDX analysis showed were comprised carbon. In this region (ca. 570 mm) the oxygen pressure was very low (Fig. 3) and carbon was able to grow on the wafer surfaces. Similar “cobbled” carbon surfaces have been described in other studies of carbon deposited from the pyrolysis of methane [20,21]. Further downstream new microstructures began to appear on the cobbled carbon surface (Fig. 6a). These structures were approximately conical in shape and increased in density until they covered the entire surface of the wafers (Fig. 4c). The morphology of the fibres varied according to the position along the reaction zone. These conical carbon fibres (CCFs) were core–shell fibres, with a silicon based core and carbon sheath. In a recent publication we have proposed that these structures grow by the action of two simultaneous processes: axial tip growth, which installs the silicon-based core, and radial thickening by pyrolytic carbon deposition [12]. This non-catalytic mechanism accounts for the conical shape of the fibres. The tip growth of the Si-based fibres supports the theory that gaseous silicon-based species form from the corrosion process upstream.

Another type of silicon–carbon structure formed under some of the test conditions was core–shell, SiO_x/carbon, fibre lattices as shown in Fig. 4d. The fibres in these lattices have a uniform diameter, and unusual fibre junctions. We have previously postulated these lattices form by a two-step process in which a silicon oxide nanowire network is first formed, and then becomes a template for pyroytic carbon deposition [11]. The junctions presumably result from both junctions in the underlying SiO_x nanowire network, and thickening of closely positioned fibres. The absence of silicon containing species on the surfaces of these structures suggests that the nanowire network forms at the beginning of the growth period, and may be a product of a period of rapid corrosion.

Under some conditions these fibre lattices were found on wafer surfaces also bearing CCFs (Fig. 6b). CCFs were occasionally found to have formed on carbon fibres, but the reverse was not observed.

Downstream of the carbon/silicon based microstructures the wafer surfaces were covered by silicon oxide nanowires (Fig. 4e). The nanowires in this region were entirely free of carbon and hence may have formed throughout the reaction and/or cooling periods. The mechanism of growth for these fibres was not determined. Nanowire growth catalyzed by metal impurities in the SiC material could not be ruled out, however, no metal particles were observed on the nanowire tips. A non-catalytic growth mechanism for silicon oxide nanowires is known [22,23].

It is clear that the core–shell carbon fibres and CCFs formed during the deposition period while both methane and oxygen were present in the gas stream. However, some structures observed on the wafer surfaces appeared to result from processes that occurred during the cooling period when the reactive gases were no longer present. These structures, which were free of carbon and comprised silicon or silicon oxide, were found on graphitic carbon surfaces. On some of the “cobbled” carbon surfaces, circular patches were observed, 0.5–5 μm in diameter, which often overlapped (Fig. 7a). EDX analysis showed that these patches contained very little oxygen.

Silicon oxide nanowire bundles were occasionally observed on the CCFs, generally close to the tips (Fig. 7b). Silicon-based rods were occasionally observed on graphitic surfaces (Fig. 7c). These relatively short rods differed from the nanowires in that they were generally straight and appeared to have a ball shaped tip, consistent with growth by the well-known vapor–liquid–solid (VLS) mechanism. The presence of these silicon-based, carbon-free structures indicates that silicon oxides continued to enter the gas phase for part of the cooling period, possibly formed by reaction of SiO_x with SiC at the SiC–SiO_x interface according to Eq. (5). While the temperature of the reactor was high this reaction could conceivably have continued in the absence of gas-phase oxidants.

To investigate the nature of the carbon deposited on the wafer surfaces Raman spectroscopy was employed. Typical Raman spectra recorded at 530, 590 and 650 mm for Expt. A are shown in Fig. 8a. Three prominent peaks were present in all spectra: D and G peaks at around 1350 and 1585 cm^{-1}, respectively, and a G' peak at 2710 cm^{-1}. D and G peaks are known to result from defect sites and sp^2 graphite, respectively [24,25]. The G' peak represents the order of crystallinity in the carbon structure [26,27]. For accuracy, the curves were fitted using Lorentzian-shaped peaks for the first order Raman spectra, and were normalized according to their peak heights at 1585 cm^{-1}. As can be seen in Fig. 8a, the intensity ratio of D to G, $R(I_D/I_G)$, and the intensity of the G' peak changed along the reactor. The intensity ratio, $R(I_D/I_G)$, based on the curve-fitting results for analyses performed along the reactor for Expt. A are also shown in Fig. 8b. The value of $R(I_D/I_G)$ was ca. 0.55 from 525 to 560 mm, after which it increased to ca. 1.1 at 605–635 mm and further to 1.4 at 660 mm. This

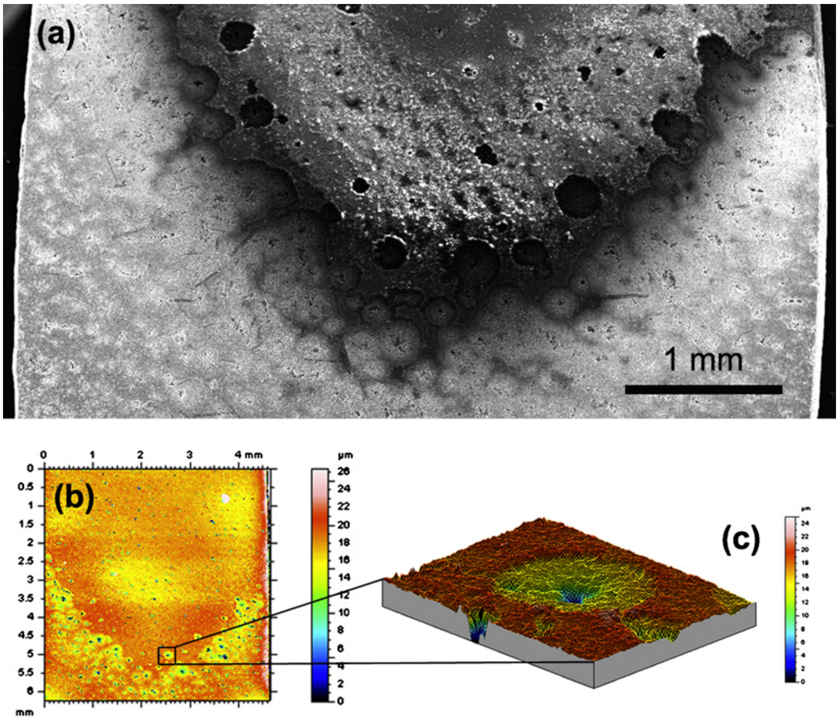

Fig. 5. An SEM image (a) and surface area map (b) of a wafer surface showing evidence of corrosion at ca. 420 mm, Expt. A. (c) Zoomed view (meshed axonometric projection) of a circular area of corrosion.

suggests that the carbon produced contained more defect sites further along the combustion zone. Corresponding to this, in Fig. 8a, the intensity of the G' peak was found to decrease on moving downstream. This can be attributed to the combined effect of temperature and the product composition of the gas stream.

In order to confirm that the microstuructures observed on the wafers were indeed a product of the combustion process, wafers which had been exposed to a 5000 sccm flow of argon at 1400 °C for 240 min were analyzed by SEM. No significant features were observed. Analysis of another set of wafers which

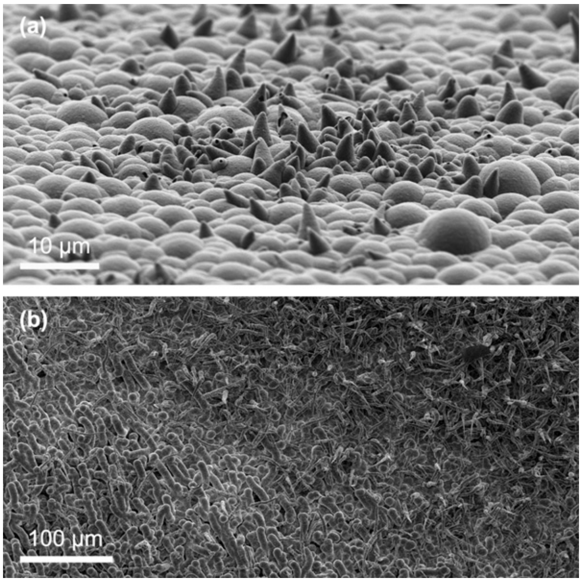

Fig. 6. (a) CCFs and “cobbled” carbon surfaces at ca. 580 mm, Expt. B. (b) A wafer surface bearing both CCFs and carbon fibres (upper right – predominantly CCFs; lower left – predominantly carbon fibres) at ca. 600 mm, Expt. B.

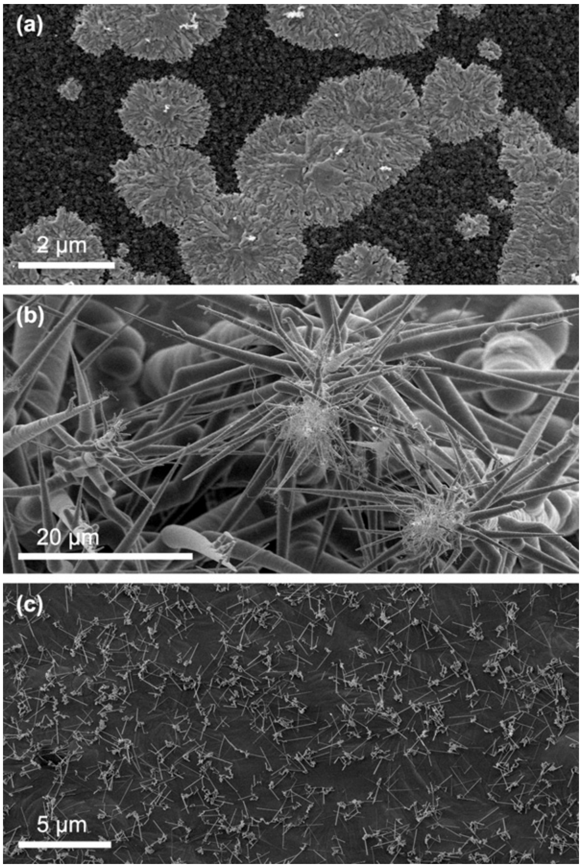

Fig. 7. Silicon containing species that were formed after reactive gases were removed from the feed. (a) Circular silicon containing patches on carbon surfaces at ca. 540 mm, Expt. B. (b) CCFs bearing bundles of SiO_x nanowires at ca. 590 mm, Expt. B. (c) Graphitic carbon surface covered by silicon-based rods at ca. 590 mm, Expt. A.

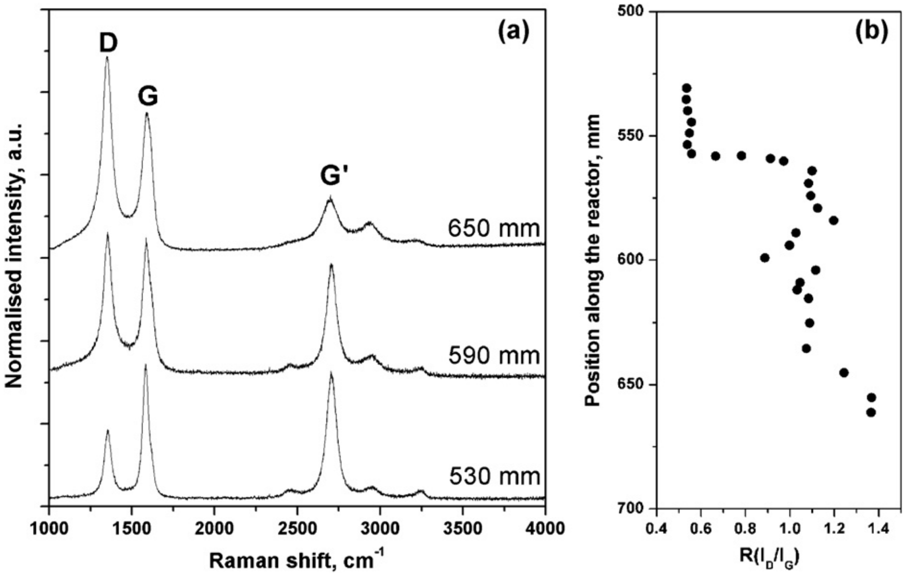

Fig. 8. Raman spectra, as a function of the position, recorded from the surface of SiC wafers used for Expt. A: (a) three representative Raman spectra for the positions of 530, 590 and 650 mm and (b) the change of $R(I_D/I_G)$ corresponding to the position along the reactor.

had been exposed to a flow of 0.9% oxygen in argon at 1400 °C revealed that silicon oxide nanowires had formed on the wafer surfaces, but that in the absence of methane no carbon species were formed.

The effect of pre-treatment of the wafers by oxidation was of interest as it appeared to be possible that pre-oxidation of the wafers might reduce or prevent microstructure formation. A set of wafers was pre-oxidized by heating in air at 1400 °C for 360 min. These wafers were then tested under the conditions described for Expt. A (Table 1). All the features observed on the wafers of Expt. A were also present the set of wafers that had been pre-oxidized, which suggests that pre-treatment, by oxidation, is unlikely to be effective in suppressing microstructure formation.

3.2.2. *Methane/oxygen ratio*

In order to investigate the effect of the CH_4/O_2 ratio on the SiC reactor surfaces a set of experiments, A–C, was designed in which all variables were held constant except for the CH_4/O_2 ratio. This ratio was set to 1:1, 1:6 and 2:1 for A, B and C, respectively, by variation of the oxygen feed partial pressure. The weight gain of the wafers for each of the experiments is shown in Fig. 9.

EDX analysis of upstream wafer surfaces, for which the weight gain was low (350–480 mm), indicated that a silicon oxide layer mainly covered the wafer surfaces. In each case the weight gain was lowest at ca. 450 mm, which correlated with the area with the most significant corrosion. Further downstream, where there was significant weight gain (500–600 mm), EDX analysis showed

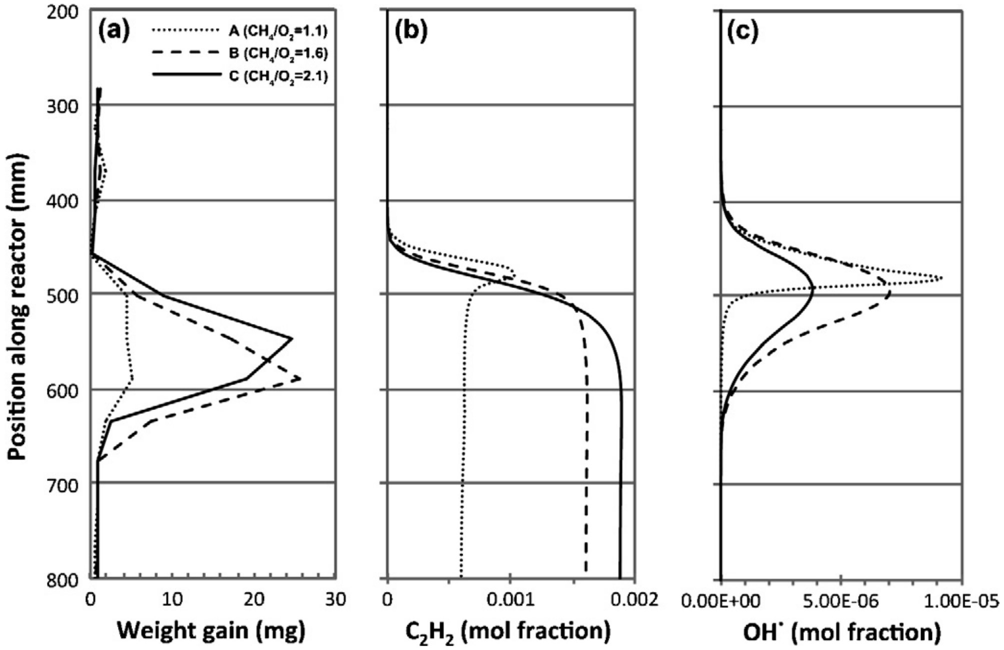

Fig. 9. Experiments conducted with CH_4/O_2 ratios of 1:1 (Expt. A), 1:6 (Expt. B) and 2:1 (Expt C): (a) the weight gain of wafers; (b) simulated C_2H_2 mole fraction along the reactor; (c) simulated hydroxyl radical mole fraction along the reactor.

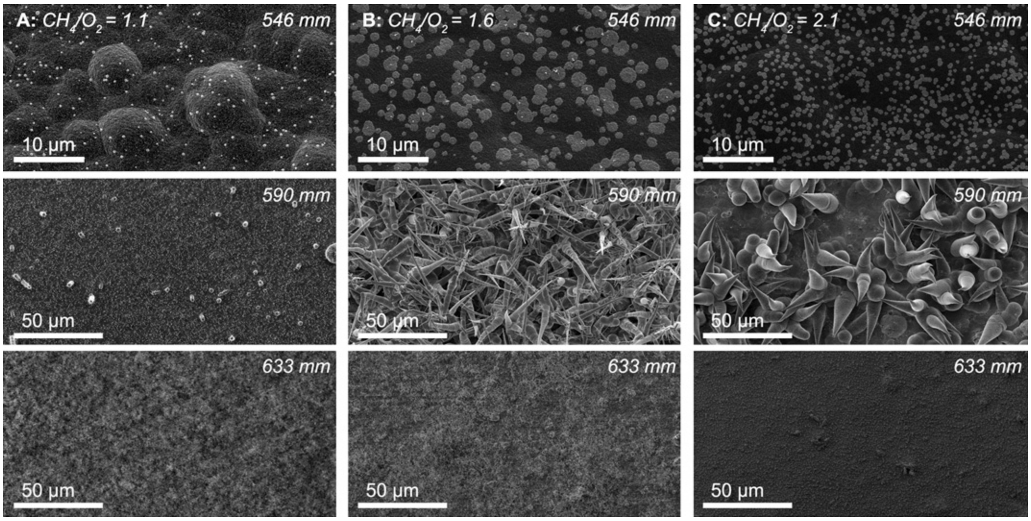

Fig. 10. SEM images of the wafer surfaces at 546, 590 and 633 mm along the reactor for experiments conducted at 1400 °C with CH_4/O_2 ratios of 1:1 (Expt. A), 1:6 (Expt. B) and 2:1 (Expt. C).

that the surfaces were mainly covered by carbon. Analysis of the product gas for each of the experiments showed that increasing the CH_4/O_2 ratio reduced the selectivity for carbon oxides and increased the selectivity for acetylene (Table 1). Fig. 9b shows the simulated acetylene mole fraction along the reactor and the measured weight gain of the wafers for each of the experiments. Acetylene is a key carbon forming species [28], and as would be expected, the increased production of acetylene at higher CH_4/O_2 ratios (as simulated and measured) was associated with an increase in the production of deposited carbon. Similar correlations were observed in simulations of other important carbon forming species such as the propargyl radical. The removal of deposited carbon would also be expected to be highest at the lowest CH_4/O_2 ratios, as the concentration of an important species that reacts with carbon, the hydroxyl radical [29,30], is higher at lower ratios, as demonstrated in Fig. 9c.

SEM analysis of the wafer surfaces from Expts. A–C demonstrated that the CH_4/O_2 ratio had a significant effect on the surface microstructures. Fig. 10 shows representative images of the wafer surfaces at specific positions along the reaction zone for each of the three experiments.

On examination of the SEM images, the effect of increasing the oxygen partial pressure appeared to be twofold, first reducing the extent of carbon deposition and second increasing the density of silicon based species. As has been discussed above, the former results from a reduction of carbon forming species in the gas phase, whereas the latter presumably results from higher oxygen partial pressures producing more corrosion of the SiC surface upstream. These trends are particularly evident from the images at 590 mm where CCFs are evident for CH_4/O_2 ratios of 1:6 and 2:1. The density of CCFs was significantly lower for the ratio of 2:1 and the tapering rate higher (tapering rate = $(r_{base} - r_{top})/l$, where r is the radius

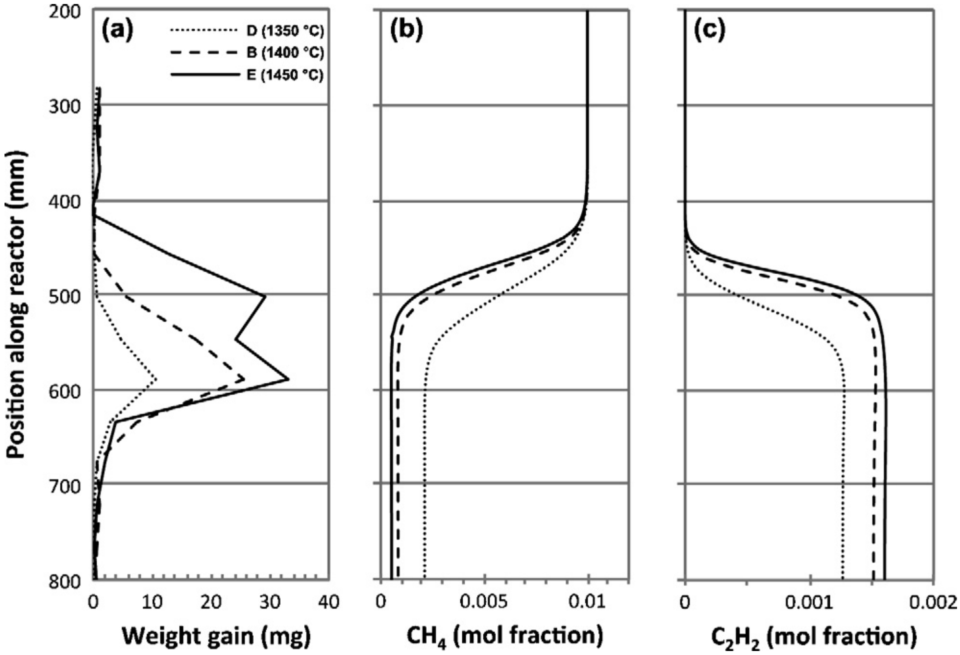

Fig. 11. Experiments conducted with the furnace temperature set to 1350 °C (Expt. D), 1400 °C (Expt. B) and 1450 °C (Expt E): (a) the weight gain of wafers; (b) the simulated CH_4 mole fraction along the reactor; (c) the simulated C_2H_2 mole fraction along the reactor.

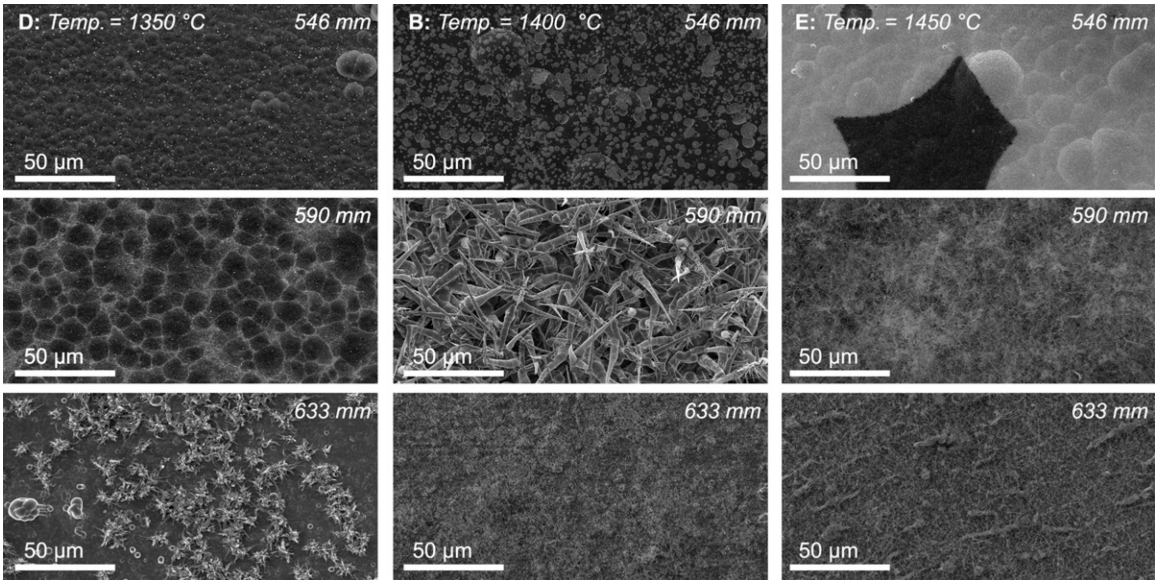

Fig. 12. SEM images of the wafer surfaces at 546, 590 and 633 mm along the reactor for experiments conducted with CH_4/O_2 ratios of 1:6 at furnace temperatures of 1350 °C (Expt. D), 1400 °C (Expt. B) and 1450 °C (Expt E).

and l the length between measurements), both of which are indicative of a lower rate of silicon-based structure growth and a higher rate of carbon deposition [12]. For the ratio of 1:1 a larger area of the wafer surfaces was covered by silicon oxide nanowires, such as those shown for 633 mm, however, at 590 mm the surface was covered by graphite and silicon-based rods as shown in Fig. 7c. In contrast, few silicon oxide nanowires were observed and at 633 mm the surface was still covered by carbon.

3.2.3. Temperature

The effect of temperature was investigated by conducting experiments with furnace temperatures of 1350, 1400 and 1450 °C, and with a CH_4/O_2 ratio of 1:6 (Expts. D, B and E, respectively). Increasing the temperature was found to both enhance the corrosion process, thus producing more silicon-based structures downstream, and increasing the extent of carbon deposition. The effect of these combined processes is apparent in the plot of weight gain of the wafers along the reactor (Fig. 11a). Also evident in this plot is a change in the position of the combustion process with increasing temperature. Wafers gained weight earlier along the reactor at higher temperatures. This behavior was also predicted by the kinetic simulations, as is evident from the plot of the simulated methane mole fraction against position along the reactor, shown for each of the three temperatures tested in Fig. 11b.

These observations were supported by SEM analyses of the wafer surfaces (Fig. 12). At 1350 °C CCFs formed further down the reactor (633 mm) than for 1400 °C (590 mm). No CCFs were formed at 1450 °C, however, the wafers were all covered by silicon containing species. Some of these silicon species, such as the surface at

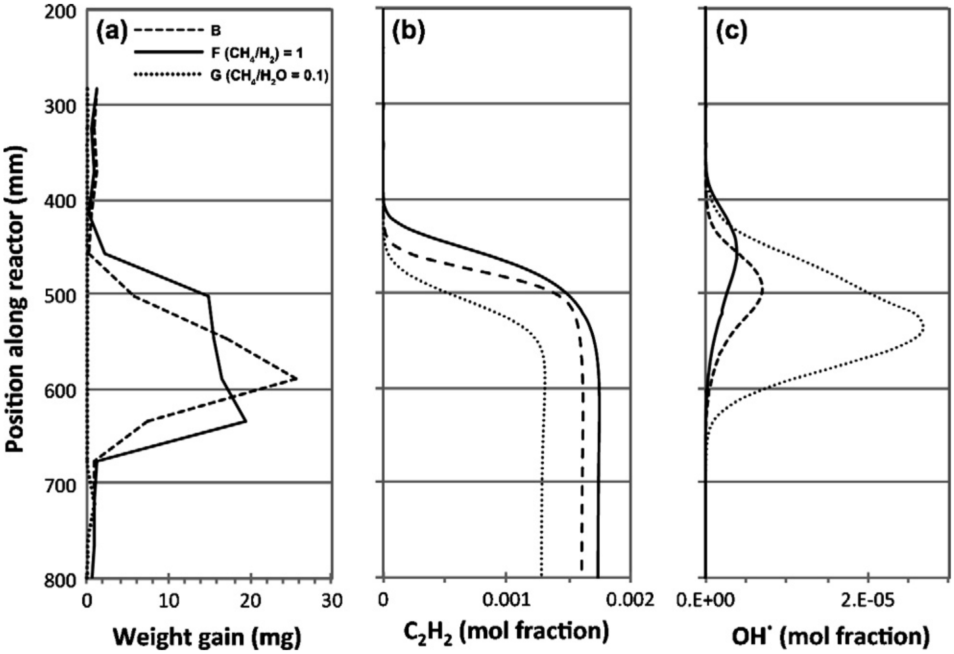

Fig. 13. Experiments conducted with no additives (Expt. B), hydrogen added (CH_4/H_2 ratio of 1, Expt. F) and water added (CH_4/H_2O ratio of 0:1, Expt. G): (a) the weight gain of wafers; (b) the simulated C_2H_2 mole fraction along the reactor; (c) the simulated hydroxyl radical mole fraction along the reactor.

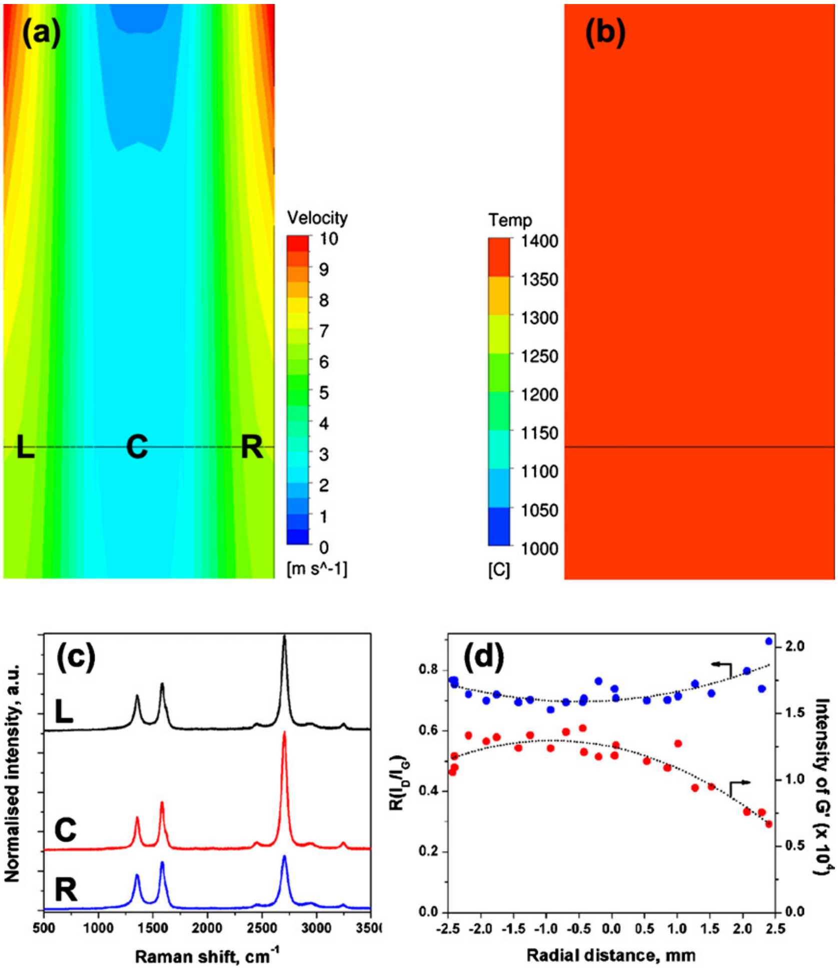

Fig. 14. Correlation between carbon structure and flow conditions using CFD and micro-Raman spectroscopy. The result of CFD simulations for: (a) the mean gas velocity; (b) the temperature at the wafer surfaces at 570–585 mm for Expt. A. (c) Raman spectra for the carbon formed on three representative regions of the wafer surface, where L = (left-hand side), C = (central region) and R = (right-hand side). (d) The intensity ratio (R) for the *D* and *G* peaks, and the intensity of the *G*′ peak radially across the wafer.

546 mm, clearly formed after the combustion period, as “cobbled” carbon surfaces are apparent under the silicon oxide layer. The processes that formed gas-phase silicon containing species during the cooling process were clearly enhanced at higher temperatures, as few silicon species were observed on the carbon surfaces of the wafers exposed to the combustion process at 1350 °C, whereas the surfaces exposed to 1450 °C were almost entirely covered by silicon containing structures.

From the acetylene concentrations measured in the product gas for each of the experiments, 0.18% for both 1350 and 1450 °C (Table 1), it is clear that at higher temperatures more of the acetylene formed was being converted to carbon. This effect was apparent but less clear from the kinetic simulations (Fig. 11c).

3.2.4. *Additives*

Water and hydrogen are often added to the feed in partial oxidation processes to suppress coking of reactors. In order to investigate the effect of these additives to the feed gas on the gas-phase and surface chemistry, Expts. B, F and G were compared. For Expt. F a CH_4/H_2 ratio of 1 was tested with a CH_4/O_2 ratio 1:6 and a furnace temperature of 1400 °C. For water a CH_4/H_2O ratio of 1 was not possible, as the experimental system was not able to accurately deliver water at a sufficiently slow rate. Therefore, for Expt. G a CH_4/H_2O ratio of 0:1 was used. The weight gain of the wafers and simulated acetylene and hydroxyl radical mole fractions along the reactor for Expts. B, F and G are shown in Fig. 13.

The addition of hydrogen or water was found to reduce both the conversion of methane and the selectivity for acetylene. The addition of hydrogen led to a decrease in the selectivity to carbon monoxide and carbon dioxide, but increased the extent of carbon deposition. In contrast, water addition increased the selectivity to the carbon oxides, particularly carbon dioxide but decreased the extent of carbon deposition significantly. The significant weight gain with hydrogen present was unexpected as hydrogen is generally thought to hinder the production of carbon forming species. It is possible that the increase in deposited carbon in the presence of hydrogen was due to a drop in the concentration of the hydroxyl radical, as can be seen in Fig. 13c. Certainly for water addition, the high concentration of the hydroxyl radical will have played an important role in reducing the extent of carbon deposition on the wafer surfaces. Very little weight gain was found for this experiment (Expt. G). Another factor that may have enhanced the carbon formation in the presence of hydrogen was that the gas phase reactions, in particular the reaction of hydrogen with oxygen, would have increased the heat produced, in comparison with the experiments with water addition and without additives. Similarly, the reduction of carbon formation on the addition of water to the feed may have also been influenced by a thermal effect. Water addition is proposed to reduce carbon formation in combustion processes as a consequence of the high heat capacity of water reducing the temperature of combustion and hence the methane conversion and carbon formation [16,29,31]. Indeed, the conversion of methane was significantly lower with water in the feed (83% vs. 92%, Table 1), lending weight to this supposition.

3.2.5. Residence time

The effect of longer residence times was investigated by exposing wafers to the same conditions as Expt. A, but with a flow rate of 2000 sccm (Expt. H), rather than 5000 sccm. The kinetic simulations of these conditions suggested that the combustion process occurred earlier along the reactor for the longer residence time (Fig. 3h). This was supported by experimental observations, with carbon observed on wafer surfaces earlier along the reactor than for Expt. H. Overall, the wafer surfaces of Expt. H were characterized by a larger proportion of carbon, consistent with longer residence times promoting carbon formation.

3.2.6. Concentration

It was of interest to determine which, if any, of the surface structures formed at low reactive gas concentrations also formed at higher concentrations. An experiment was conducted with a methane concentration of 10% (Expt. I), and efforts were made to ensure that the results could be compared to Expt. A. To achieve this it was necessary to use a lower furnace temperature, as the heat of reaction with 10% methane was significant. Without wafers various furnace temperatures were run and the peak reactor temperature recorded. The furnace temperature required to match the peak reactor temperature for the 10% methane feed with the Expt. A (furnace temp. = 1400 °C) was found to be 1275 °C, and this furnace temperature was then used with wafers. Inspection of the wafer surfaces by SEM revealed that from ca. 450 to 650 mm the wafer surfaces were coated with "cobbled" carbon. No significant silicon/carbon microstructures were observed; although upstream of the "cobbled" carbon the surfaces of the wafer surfaces did appear to be corroded, suggesting that silicon based species had entered the gas phase.

3.2.7. Fluid flow

As described in Section 3.1.1, the wafer configuration inside the reactor produced a complex flow pattern in the microstructure growth region. Throughout the analytical work efforts were made to determine whether the fluid flow played any role in the microstructure formation. Overall no significant effect was observed, however, one interesting observation was made during a micro-Raman spectroscopic analysis of the carbon covered wafer surfaces from Expt. A. Fig. 14a and b shows the results of a CFD simulation for the mean gas velocity and temperature for the gas flow at the wafer surface from 570 to 585 mm. In this region the mean gas velocity was greater close to the edge of the wafer while the surface temperature was constant. In Fig. 14c, Raman spectra for three different regions are presented. The carbon on the central region of the wafer (C in Fig. 14a and c) produced a more intense G' peak in Raman spectrum than that from edge regions (L and R). This indicates that the carbon formed on the central surface region of the wafer contained a more highly ordered graphitic structure. This was further confirmed by Fig. 14d, which shows the intensity ratio of D and G peaks, $R(I_D/I_G)$, and the intensity of the G' peak, $I_{G'}$, from Raman spectra recorded radially across the wafer. On moving from the edge towards the central region of the wafer, $R(I_D/I_G)$ decreased whereas $I_{G'}$ increased.

This combination of CFD modeling and Raman analysis suggests that the carbon structure can be affected by the flow conditions. The exact reason for this effect is unclear, however, it may be associated with a higher rate of carbon formation at the edge of the wafers, where the gas flow rate is higher.

4. Conclusions

The results of this study clearly demonstrate that corrosion of SiC surfaces exposed to the partial oxidation of methane produces silicon-based species that enter the gas phase, and that a transport mechanism exists which enables the movement of these species away from the corrosion zone. Furthermore, it is evident that under certain conditions the gas-phase silicon species can deposit on the surfaces downstream of the corrosion zone, forming either silicon-based or silicon/carbon based nano- or microstructures. Silicon/carbon microstructures appear to form in a region towards the end of the combustion zone, i.e. where gaseous carbon forming species are present in relatively high concentrations and oxygen at low concentration, and the temperature is high. Silicon-based nano-structures form downstream of the silicon/carbon structures, where combustion is complete, but the temperature is still high.

Nano- and microstructure formation is clearly exacerbated by certain process variables. In particular, high temperatures and low methane/oxygen ratios enhanced the formation of silicon-based structures, while high temperatures, higher methane/oxygen ratios and lower flow rates enhanced carbon deposition. Water addition added at a CH_4/H_2O ratio of 0.1 significantly reduced deposited carbon formation, whereas surprisingly, hydrogen addition did not appear to reduce the selectivity for deposited carbon. The reactive gas concentration also appears to be a crucial factor. When the reactive gas concentration was increased for 1–10%, only flat graphitic surfaces formed. Consequently particular attention should be paid for SiC devices in which combustion occurs under dilute conditions.

There appears to be a weak link between the complex flow pattern, as predicted by the CFD simulation, and the microstructure formation on some parts of the wafers. A more targeted investigation would be needed to ascertain this finding.

During this study it also became apparent that silicon nanowire formation occurred both on exposure of SiC to methane combustion processes, and on exposure to oxygen alone. An in depth study of nanowire formation on SiC surfaces exposed to oxidizing environments will be described in a forthcoming publication.

In this study no conclusions could be drawn regarding the mechanism for silicon-based fibre formation. Non-catalytic growth mechanisms for silicon-based fibres are known, but the action of metal catalyzed growth could not be ruled out in this study. Metal catalyzed nano- and microstructure growth is likely to become more problematic when SiC is used as a support material for heterogeneous catalysts. This is an area that requires further investigation and is the focus of current studies.

Acknowledgements

The authors would like to thank: Mr. Merrill Wilson and Mr. James Cutts (Ceramatec Inc.) for providing ceramic materials and advice; Mr. Mark Greaves and Ms. Lisa Wong (CSIRO) for assistance with SEM studies; Ms. Karen Hands (CSIRO) for assistance with surface area structure analyses; Prof. Peter Glarborg (Technical University of Denmark) for supplying a CHEMKIN formatted version of the combustion mechanism used in kinetic simulations.

References

[1] L.J. Velenyi, Y. Song, J.C. Fagley, Ind. Eng. Chem. Res. 30 (1991) 1708–1712.
[2] G.J. Heynderickx, G.F. Froment, P.S. Broutin, C.R. Busson, J.E. Weill, AIChE J. 37 (1991) 1354–1364.
[3] A. Wörner, R. Tamme, Catal. Today 46 (1998) 165–174.
[4] J. Coronas, M. Menendez, J. Santamaria, Ind. Eng. Chem. Res. 34 (1995) 4229–4234.
[5] S. Tacchino, L.D. Vella, S. Specchia, Catal. Today 157 (2010) 440–445.
[6] Christian, M. Mitchell, D.P. Kim, P.J.A. Kenis, J. Catal. 241 (2006) 235–242.
[7] M.J. Ledoux, C. Pham-Huu, CATTECH 5 (2001) 226–246.

[8] C. Méthivier, B. Béguin, M. Brun, J. Massardier, J.C. Bertolini, J. Catal. 173 (1998) 374–382.
[9] R.J. Shang, Y.Y. Wang, G.Q. Jin, X.Y. Guo, Catal. Commun. 10 (2009) 1502–1505.
[10] X. Guo, G. Zhi, X. Yan, G. Jin, X. Guo, P. Brault, Catal. Commun. 12 (2011) 870–874.
[11] W.J. Lee, C. Li, N. Burke, D. Trimm, J. Patel, Carbon 49 (2011) 1167–1172.
[12] W.J. Lee, C. Li, N. Burke, D. Trimm, J. Patel, Carbon 49 (2011) 2735–2741.
[13] F. Menter, T. Esch, in: Proceedings of COBEM, Uberlandia, Brazil (2001).
[14] C.P. Yorke, G.N. Colemaan, Eur. J. Mech. B-Fluid 23 (2004) 319–337.
[15] G.G. Kanaris, A.A. Mouza, S.V. Paras, Chem. Eng. Res. Des. 83 (2005) 460–468.
[16] M.S. Skjøth-Rasmussen, P. Glarborg, M. Østberg, J.T. Johannessen, H. Livbjerg, A.D. Jensen, T.S. Christensen, Combust. Flame 136 (2004) 91–128.
[17] Gregory P. Smith, David M. Golden, Michael Frenklach, Nigel W. Moriarty, Boris Eiteneer, Mikhail Goldenberg, C. Thomas Bowman, Ronald K. Hanson, Soonho Song, William C. Gardiner Jr., V.V. Lissianski, Z. Qin, http://www.me.berkeley.edu/gri_mech/.
[18] J. Wang, L. Zhang, Q. Zeng, G.L. Vignoles, A. Guette, J. Am. Ceram. Soc. 91 (2008) 1665–1673.
[19] V. Presser, K.G. Nickel, Crit. Rev. Solid State Mater. Sci. 33 (2008) 1–99.
[20] E.A. Blekkan, R. Myrstad, O. Olsvik, O.A. Rokstad, Carbon 30 (1992) 665–673.
[21] S.H. Liu, F. Li, S. Bai, J. Mater. Sci. Technol. 25 (2009) 259–263.
[22] N. Wang, Y. Cai, R.Q. Zhang, Mater. Sci. Eng. R-Rep. 60 (2008) 1–51.
[23] R.Q. Zhang, Y. Lifshitz, S.T. Lee, Adv. Mater. 15 (2003) 635–640.
[24] F. Tuinstra, J.L. Koenig, J. Chem. Phys. 53 (1970) 1126.
[25] D.S. Knight, W.B. White, J. Mater. Res. 4 (1989) 385–393.
[26] M. Endo, C. Kim, T. Karaki, T. Kasai, M.J. Matthews, S.D.M. Brown, M.S. Dresselhaus, T. Tamaki, Y. Nishimura, Carbon 36 (1998) 1633–1641.
[27] T.V. Reshetenko, L.B. Avdeeva, Z.R. Ismagilov, V.V. Pushkarev, S.V. Cherepanova, A.L. Chuvilin, V.A. Likholobov, Carbon 41 (2003) 1605–1615.
[28] M. Frenklach, Phys. Chem. Chem. Phys. 4 (2002) 2028–2037.
[29] B.S. Haynes, H.G. Wagner, Prog. Energ. Combust. 7 (1981) 229–273.
[30] I.M. Kennedy, Prog. Energ. Combust. 23 (1997) 95–132.
[31] K.P. Schug, Y. Manheimertimnat, P. Yaccarino, I. Glassman, Combust. Sci. Technol. 22 (1980) 235–250.